Computational modelling and simulation of cancer growth and migration within a 3D heterogeneous tissue: the effects of fibre and vascular structure

Cicely K Macnamara[a,*], Alfonso Caiazzo[b], Ignacio Ramis-Conde[c], Mark AJ Chaplain[a]

[a] *School of Mathematics and Statistics, Mathematical Institute, University of St Andrews, United Kingdom, KY16 9SS*
[b] *Weierstrass Institute for Applied Analysis and Stochastics (WIAS) Leibniz Institut im Forschungsverbund Berlin e.V., Berlin, Germany*
[c] *Universidad de Castilla la Mancha, Departamento de Matemáticas, Facultad de Educación, Cuenca, Spain*

Abstract

The term cancer covers a multitude of bodily diseases, broadly categorised by having cells which do not behave normally. Since cancer cells can arise from any type of cell in the body, cancers can grow in or around any tissue or organ making the disease highly complex. Our research is focused on understanding the specific mechanisms that occur in the tumour microenvironment via mathematical and computational modeling. We present a 3D individual-based model which allows one to simulate the behaviour of, and spatio-temporal interactions between, cells, extracellular matrix fibres and blood vessels. Each *agent* (a single cell, for example) is fully realised within the model and interactions are primarily governed by mechanical forces between elements. However, as well as the mechanical interactions we also consider chemical interactions, for example, by coupling the code to a finite element solver to model the diffusion of oxygen from blood vessels to cells. The current state of the art of the model allows us to simulate tumour growth around an arbitrary blood-vessel network or along the striations of fibrous tissue.

Keywords: cancer modelling; individual-based model; cell-matrix interaction; vasculature; finite element method

*Corresponding author
Email addresses: ckm@st-andrews.ac.uk (Cicely K Macnamara), caiazzo@wias-berlin.de (Alfonso Caiazzo), ignacio.ramis@uclm.es (Ignacio Ramis-Conde), majc@st-andrews.ac.uk (Mark AJ Chaplain)

1. Introduction

Cancer Research UK estimates that approximately 50% of the UK's population will receive a cancer diagnosis during their lifetime [3], and as the second-leading cause of death worldwide the World Health Organisation reports that one in six deaths will be caused by it [16]. The term cancer covers a multitude of diseases, broadly categorised by having cells which do not behave normally. Since cancer cells can form from any type of cell in the body, cancers can arise from and grow in any tissue or organ making the disease highly complex. Moreover, ideally, treatment for cancer should target the tumour cells while having limited or no effect on the surrounding healthy cells and tissue microenvironment. One of the *Hallmarks of Cancer* [24, 25] is tissue invasion and metastasis. Tumour cells proliferate and occupy whole areas of tissue. Additionally they interact with surrounding cells, tissue structures, vasculature and the extracellular matrix in a variety of ways. While some cancer behaviour is well understood (such as avascular growth and tumour angiogenesis) we are yet to elucidate all of the mechanisms by which cancer cells take hold of, use, and affect the body. Mathematical modelling and simulation can complement traditional biological and experimental approaches to cancer research.

Mathematical modelling of biological processes and systems can trace its roots back over 100 years to the seminal work of D'Arcy Thompson "*On Growth and Form*" [43]. More recently, in the past twenty five years or so, there has been increased interest in the mathematical modelling of cancer growth and treatment, leading to the development of a field in its own right - *mathematical oncology*. Much of this research focuses on the interaction of cancer cells with their local tissue, "the tumour microenvironment". At the same time, there has also been increased interest in computational tools and simulation techniques, so called *in silico* models, which aim to provide the biologist with additional insight without potentially high economic, time and ethical costs. Cancer research is a prime example of a field for which the use of *in silico* modelling is gathering pace. One particular branch of *in silico* models for solid tumours, and of particular interest here, is that of agent-based models. For a review of cell-based computational modelling in cancer biology see [34]. In an agent- or individual-based (IB) model one seeks to learn more about the whole system under study by examining the actions and interactions of its individual parts or components. An IB model of a solid tumour may reproduce the behaviour of various tumour components, for example, the individual cancer cells; the vessels forming the tumour vasculature and components of the tumour microenvironment. It is precisely such a model which we present here.

IB modelling of such a complex system as a solid tumour is certainly an ambitious approach, since there will be a large number of parameters and variables across multiple scales. However, implementing these realistic models offers a constructive tool that truly complements experimental methods. In clinical and experimental practice, scientists are able to track only a limited number of parameters using specific and well established markers. On the one hand, this *top-down* approach (from macroscopic markers to microscopic biological

parameters) ensures that the model reproduces the major biological processes. On the other hand, as the number of variables is very large (in the form of cells, proteins, particles or similar complexes and interactions between them), the complexity reduction might yield a large amount of side masking effects. Multiscale and IB modelling offers a *bottom-up* approach that, starting from the processes at the level of individual cells, has the capability to isolate a small number of variables and can complement real and macroscopic observations.

Due to the realistic simulations they offer, IB models are now used widely within mathematical oncology and in many other areas of biomedical systems research. Here we focus particularly on a model of solid tumour growth but other researchers have used and are using IB models to look at tumour-immune interactions (e.g., [35, 28, 29, 30]), invasion (e.g., [1, 46, 39]) and metastatic spread (e.g., [2, 19]). Our model is a force-based (centre-based) lattice-free model, and much pioneering work in this area has been carried out by Drasdo and colleagues (see, e.g., [13, 21, 14, 38]). Other authors working in this area include [31, 8, 9, 10]. For a comprehensive review of IB force-based models of tumour growth see [44] and references therein.

In this paper we present a summary of the development of the IB force-based model presented in [6]. The model presented there had previously been developed from a 2D model first presented in [38] and developed in [40, 41]. In this paper, by presenting examples of different simulations for cancer related scenarios we show the diversity and current state-of-the-art of the code. In Section 2 we give a detailed overview of the governing equations and mechanisms governing the cells within the model. The main improvements to the model concern the introduction of interactions with a vasculature network (Section 3) and fibrous tissue (Section 4). In Section 3 we show how a growing solid tumour interacts with pre-existing vasculature and how diffusion of oxygen from the blood vessel network affects the growth of the cancer cells. As discussed in this Section the underlying computational code has been developed in two particular ways. Firstly, vessels are modelled explicitly in the IB model, and this means that tumour cells can adhere to vessels and that the model can take into account a physical force between vessels and cells. Secondly, the coupling of the IB model with a continuum model for oxygen diffusion (using a finite element approach) has been improved in several ways: (i) using a more realistic non-linear reaction model; (ii) using an adaptive mesh, refined near the vessels; (iii) dynamical evaluation of when a new solution of the diffusion equation is needed, based on the variation in cell density; (iv) using Robin boundary conditions at the boundary of the continuous domain, in order to account for a more realistic effect of the surrounding tissue. In Section 4 we show how the growth of a tumour mass is affected by the local tissue structures; how its shape is altered by the alignment of extracellular matrix (ECM) fibres. The model has been developed to include the fibres as additional agents in order to take into account the mechanical interplay between fibres and cells. We note that in the previous work of [40] fibres were also incorporated. However, the model presented there is 2D, and in this current paper moving to a 3D domain has added significantly to the complexity of the cell-fibre interactions. In Section 5 we summarise the

current capabilities of the model and discuss plans for further development of the code.

2. Individual-based model of cancer growth

In this Section we describe our model for solid tumour growth. Specifically, since we employ an IB approach, each cancer cell is considered to be an agent that grows, divides, acquires a certain phenotypic status and interacts with other neighbouring cells (and later in the paper, with both blood vessels and individual fibres constituting the ECM). We will focus first on describing the cell-cell interactions. As discussed in the introduction, this is a force-based model and so the interactions are primarily mechanical and each cell is governed by an equation of motion.

2.1. The equation of motion

Firstly, we note that we model each cell as a viscoelastic sphere subjected to small deformations. It is true that the shape of cancer cells can vary depending on the type of tumour, environment and on the degree of differentiation. Furthermore, individual cellular behaviour at the tumour interface is dependent on specific molecular-scale interactions that result in cytoplasmic deformations. However, when a growing solid tumour (which reaches a size consisting of thousands of individual cells) it is acceptable to make this simplification on the cell geometry (i.e. spherical cells). Formally, then, each cell is described by a set of state variables including the cell centre position, $\mathbf{x}$, cell radius, (r), cellular phenotype, σ, oxygen concentration, $c(\mathbf{x},t)$ and the stage in the cell cycle, η. Cell dynamics are governed by the following set of ordinary differential equations (one for each cell):

$$\underbrace{\mathbf{\Gamma}\mathbf{v}_i(t)}_{\text{friction}} + \underbrace{a^r f_i(t)}_{\text{random fluct.}} = \underbrace{\sum_{j=1}^{N_{\text{cells}}(t)} \mathbf{F}_{i,j}(t)}_{\text{cell-cell forces}}, \tag{1}$$

where $\mathbf{v}_i = \dot{\mathbf{x}}_i$ denotes the velocity of cell i and $\mathbf{\Gamma}$ is a 3-dimensional tensor that models the physical structure of the environment, for simplicity assumed to be isotropic, i.e., $\mathbf{\Gamma}_{l,k} = \gamma\delta_{l,k}$. The term $a^r f_i(t)$, where f_i is a normal function with zero mean and unit variance, models the active random forces exerted by cellular mechanisms as a process of exploration of the nearby space, as well as other normally distributed spatial fluctuations that may happen at the cellular scale [22]. Finally, $N_{\text{cells}}(t)$ denotes the total number of cells at time t and $\mathbf{F}_{i,j}(t)$ is the force exerted on a cell i by a neighbouring cell j, consisting of a combination of repulsive and attractive forces (see Section 2.2).

We solve the model numerically based on an explicit discretisation of (1), where the cell position is computed, at time t^{n+1}, via

$$\mathbf{x}_i(t^{n+1}) = \mathbf{x}_i(t^n) + \frac{\Delta t}{\gamma}\left(-a^r f_i(t^n) + \sum_{j=1}^{N_{cells}(t^n)} \mathbf{F}_{i,j}(t^n)\right), \tag{2}$$

where Δt denotes the time step.

2.2. Cell-cell interaction

This Section briefly describes the forces governing the cell-cell interactions. For more details on this, we refer the reader to [6]. An interaction is assumed to only take place between two cells in contact with each other, and is composed of both a repulsive and an adhesive component. Let us consider two cells (denoted by i and j), let R_i and R_j be their radii, and let $\mathbf{d}_{ij}$ denote the spatial vector connecting their cell centres, oriented from the centre of cell i to the centre of cell j. In what follows, we will consider the case $|\mathbf{d}_{ij}| \leq R_i + R_j$, i.e., when the cells are in contact, introducing also the length of "overlap" between cells given by

$$h_{ij} = R_i + R_j - \|\mathbf{d}_{ij}\|. \tag{3}$$

Denoting with E_i and E_j the cells' Young's moduli and with ν_i and ν_j their Poisson ratios, the repulsive force term, $\mathbf{F}^{\text{rep}}_{i,j}$, is computed from the Hertz model [27] (assuming sufficiently small deformations) and is given as

$$|\mathbf{F}^{\text{rep}}_{i,j}| = \frac{4}{3} E^* {R^*}^{1/2} {h_{ij}}^{3/2}. \tag{4}$$

In (4), $R^* = R_i R_j/(R_i + R_j)$ is the effective radius and E^* is the effective Young's Modulus calculated from

$$\frac{1}{E^*} = \frac{1-\nu_i^2}{E_i} + \frac{1-\nu_j^2}{E_j}. \tag{5}$$

The adhesion force between cells is produced by adhesive molecules that travel to the cellular membrane, stimulated by the the proximity of the neighbouring cell. Therefore, the adhesion force, $\mathbf{F}^{\text{adh}}_{i,j}$, between two overlapping cells, is assumed be proportional to the contact surface between them, denoted by S_{adh} [37]. Since we assume small cell deformations, the contact surface between the two cells is computed as the average value between the area of a spherical cap of height the overlap between the cells, h_{ij}, and surface of the circle underlying the cap. Thus,

$$S^{\text{adh}}_{ij} = \frac{1}{2}\left[2\pi R_i h_{ij} + \pi\left(R_i^2 - (R_i - h_{ij})^2\right)\right] \tag{6}$$

yielding the force

$$|\mathbf{F}^{\text{adh}}_{i,j}| = \alpha^* \left(R_i - \frac{h_{ij}}{4}\right) h_{ij}. \tag{7}$$

In (7), $\alpha^* = 2\pi\alpha$, and α is the adhesion constant, which is currently assumed to be constant among the cell population. Note that this adjusted adhesion coefficient α^* will be referred from here on as the adhesion coefficient. The advantage of using this adhesion approach (instead of a linear term as in [38]) resides in the fact that it considers a suction effect as a consequence of the increasing density of effective bonds between the cells.

The total cell-cell interaction force is directed along the vector joining the centres of cells i and j, it is

$$\mathbf{F}_{i,j} = \left(\mathbf{F}_{i,j}^{\text{rep}} - \mathbf{F}_{i,j}^{\text{adh}}\right) \frac{\mathbf{d}_{ij}}{\|\mathbf{d}_{ij}\|} \tag{8}$$

and can be determined using equations (4) and (7). Notice that in equation (8) we assume, without loss of generality, that positive forces for cell i are directed outwards.

For the simulations shown in this paper we shall suppose that all cells have the same maximum radii, Young's moduli, Poisson ratios and adhesion constant, denoted by R, E ν and α^*, respectively. The values for the parameters used in model Equation (2) are given in Table 1 (see also [6, 38, 37]). With these choices, the potential is minimised (and thus forces are in equilibrium) when cell centres are approximately 8.5μm apart, causing a small deformation to the spherical cell.

Parameter	Description	Value
R	maximum cell radius	5μm
E	Young's modulus	$1e{-}3\mu\text{N}/\mu\text{m}^2$
ν	Poisson ratio	0.5
α^*	adhesion coefficient	$3.72e{-}4\mu\text{N}/\mu\text{m}^2$
Δt	timestep	1 min
γ	cell-medium friction constant	$0.01\mu\text{N}\mu\text{m}/\text{min}$
a^r	amplitude of random forces	$4 \times 10^{-3}\mu\text{N}$

Table 1: Parameter values for Equation (2) used in the simulations throughout this paper.

2.3. Cell cycle, growth and birth

Besides the mechanical interactions between cells, cells are also subject to changes due to biological factors, such as the cell cycle, mitosis and mutations. Mitosis is modeled by a combination of processes, depending on three necessary biological conditions and a probability distribution.

The necessary conditions are:

(1) Cells are allowed to undergo mitosis only after reaching the mature state. The cell cycle is modeled by assuming that each cell increases in size at a given growth rate (specifically, $0.1\,\mu$min) until it achieves a prescribed maximum radius, $R\mu$m. Once the cell has grown to its proliferating size (at least 99% of this maximum) the condition is satisfied.

(2) Cells are allowed to undergo mitosis only if contact inhibition processes are not activated. Mitosis is not possible if the cell experiences an excessive compression force due to the neighbouring cells. To take this into account, mitosis is only allowed as long as (i) the repulsive force of the modified

Hertz model (see Equation (4)) is below a given threshold $F^*_{c,m}$[1], and (ii) the number of total contact neighbours of the cell is below a given threshold $n^*_{c,m}$ (approximately 16 neighbours, as in [6, 37]).

(3) Cells are allowed to undergo mitosis only if there is enough oxygen in the surrounding media. This last condition depends on the type of scenario to be modeled. Cells can have different phenotypes, depending on the problem under consideration, as a function of the environment surrounding the cell and/or on the cell status. A change in phenotype may manifest in a change of cell behaviour (for example, in Section 3.3.1, condition 3 is considered to be satisfied when phenotypic expression is normoxic). Cell evolution might also depend on several additional biophysical processes, such as the availability of nutrients (see Section 3) or the structure of the extra-cellular matrix (see Section 4).

When the conditions are satisfied, mitosis may occur with an uniform probability distribution with $p_{\text{mitosis}} = \frac{1}{T_{CC}}$, i.e., equal to the inverse of the cell cycle time T_{CC}. In the simulations presented in this article, T_{CC} is equivalent to 1,000 timesteps or approximately 16.5 hours.

Remark 1. *Notice that, in the proposed model, growth rate is independent of nutrient concentration. Scarcity of nutrient does affect the phenotypic state o a cell, which has a direct influence on both its oxygen uptake/consumption and mitosis (see condition (3)).*

2.4. Implementation details

The individual cell model has been implemented in a C++ solver, in which each cell is an independent object with a given set of properties (radius, position, phenotype, etc.). Each iteration is composed of a *global* step, in which each `Cell` obtains information about its neighbours, and a *local* step, comprising all operations that are performed cell by cell (computing forces and velocities, mitosis, mutations). The domain is divided into boxes, and each cell is uniquely assigned to the box containing its centre. This subdivision speeds up the search for neighbours of a given cell, by restricting the operations to the cells in the neighbouring boxes.

In [6] solid tumour growth was simulated, and the model was given as above but the tumour grew within a domain diffused with oxygen from "vessel" sources. In the next Section we develop this approach by introducing additional agents (vessels) so that we may model mechanical as well as chemical interactions between solid tumours and a pre-existing vasculature.

[1] The threshold force is currently calculated as the value of the repulsion force of 12 cells at a contact distance of 8.5μm

3. Growth Around Blood Vessels

This Section describes in detail the coupling between the IB model described in Section 2 and updated to include an IB treatment of the vessels, with a finite element solver for simulating oxygen diffusion within the tissue.

In order to setup an efficient computational approach, we consider an extension of the multiscale model recently proposed in [6]. Namely, we simulate oxygen diffusion within the tissue solving a reaction-diffusion equation with a finite element method, in which the vascular tree is taken into account as an immersed singular source. As observed in [6], this approach allows us to efficiently treat arbitrary vascular structure, without the need of adapting the finite element mesh.

3.1. Mathematical Model

Oxygen uptake is a variable of extreme importance when determining the dynamics of cancer growth. Depending on availability of oxygen in the surrounding tissues, cancer cells might undergo different biophysical processes. In the case of hypoxia (lack of oxygen), cancer cells typically increase their motility but eventually, as oxygen levels continue to drop, become necrotic. As oxygen is provided by the blood vessels perfusing the tissue, understanding the interplay between cancer cells, cancer growth and vasculature is crucial.

To formulate the model, let us denote with $\Omega \subset \mathbb{R}^3$ the space occupied by the whole tissue domain and by Ω_v the domain of blood vessels. The oxygen concentration is governed by the following reaction-diffusion equation and boundary conditions assuming that oxygen diffuses within the cellular tissue homogeneously with a known diffusion constant.

$$\begin{cases} \partial_t c - D_{O_2}\Delta c + \dfrac{\alpha_n\rho_n + \alpha_h\rho_h}{c^{(T)} + c}c = 0, & \text{in } \Omega, \\ \dfrac{\partial c}{\partial \mathbf{n}} = \phi_v = \dfrac{1}{J_v}(c_v - c), & \text{on } \partial\Omega_v, \\ \dfrac{\partial c}{\partial \mathbf{n}} = \dfrac{1}{\eta D_{O_2}}\left(c_{+\infty} - c\right), & \text{on } \partial\Omega/\partial\Omega_v, \end{cases} \tag{9}$$

where $c(\mathbf{x}, t)$ denotes the oxygen concentration. In the reaction-diffusion equation $(9)_1$, D_{O_2} is the diffusion coefficient of oxygen, ρ_n and ρ_h stand for the density of normoxic and hypoxic cells, respectively, α_n and α_h are model parameters regulating oxygen uptake and $c^{(T)}$ is the saturation constant (the oxygen level at which the consumption rate is halved). The last term on the left-hand side models the oxygen/nutrient uptake by different cell types, modelled through Michaelis-Menten type kinetics. The boundary conditions are of Robin-type. Equation $(9)_2$ models the filtration from vessels to tissue, while Equation $(9)_3$ imposes a condition on the external boundaries of the tissue sample, i.e. those boundaries not adjacent to any vessel wall. In particular, we consider that blood vessels are sources of oxygen, from which oxygen is constantly diffused into the domain at a rate ϕ_v, based on a filtration law in which c_v denotes the oxygen

partial pressure inside the vessel and J_v is the filtration coefficient (assumed to be known). In this way the oxygen flux, ϕ_v, through the boundary, $\partial\Omega_v$, is assumed to be proportional to the concentration difference between the vessel and the tissue. We consider $c_{+\infty}$ to be a far field partial pressure. Notice that small values of the model parameter η corresponds, from a mathematical point of view, to imposing $c = c_{+\infty}$ i.e. a Dirichlet boundary condition, while large values of η or $c_{+\infty} = 0$ are both equivalent to imposing a homogeneous Neumann boundary condition.

Equation $(9)_1$ is a time-dependent non-linear partial differential equation for the concentration $c(\mathbf{x}, t)$. In order to obtain an efficient solution method, within our computational model we considered the following hypothesis. Firstly, we assume a strong scale separation between the oxygen diffusion (time to reach an equilibrium state) and the cellular tissue growth. Hence, for the purposes of the coupled model equation $(9)_1$ can be replaced by its steady counterpart

$$-D_{O_2}\Delta c + \frac{\alpha_n \rho_n(\hat{t}_m) + \alpha_h \rho_h(\hat{t}_m)}{c^{(T)} + c} c = 0, \quad \text{in } \Omega \tag{10}$$

where $\hat{t}_m$ denotes the m-time iteration in the time scale of the cells, and specifies the current cell configuration.

Secondly, we assume that the oxygen distribution does not change excessively from one iteration of the diffusion solver to another (provided the cell distribution remains close). This assumption is used to linearise the reaction terms in equation (10), replacing the unknown concentration c at a time iteration $\hat{t}_m$ with the previously calculated $c(\hat{t}_{m-1})$. Hence, the continuum equation that is considered for the coupling with the individual-based model is given by

$$-D_{O_2}\Delta c + \frac{\alpha_n \rho_n(\hat{t}_m) + \alpha_h \rho_h(\hat{t}_m)}{c^{(T)} + c(\hat{t}_{m-1})} c = 0, \quad \text{in } \Omega. \tag{11}$$

3.2. Finite element approximation

In order to solve equation (11) numerically, we consider a tetrahedral mesh $\mathcal{T}_h$ of the computational domain Ω and the discrete (finite element) space $V_h = \mathbb{P}_2(\mathcal{T}_h)$ of the piecewise quadratic functions on the elements of $\mathcal{T}_h$. Moreover, let us denote with $(\cdot,\cdot)_\Omega$ the standard L^2 scalar product defined by

$$(p, q)_\Omega = \int_\Omega pq \, d\Omega$$

for all $p, q \in V_h$.

The finite element method for the diffusion equation (11) is derived starting from its weak formulation. Namely, we first multiply equation (11) by an arbitrary function $q \in V_h$ (a so-called *test function*) and then integrate by parts,

obtaining the following equivalent problem: Find $c \in V_h$ such that

$$(D_{O_2}\nabla c, \nabla q)_\Omega + \sum_{\alpha=N,H} (\mu_\alpha R_\alpha^{cells}(t^{cells})c, q)_\Omega + \underbrace{\left(\frac{1}{J_v}(c - c_v), q\right)_{\partial\Omega_v}}_{\Phi_v} + \left(\frac{1}{\eta D_{O_2}}(c - c_{+\infty}), q\right)_{\partial\Omega\setminus\partial\Omega_v} = 0, \tag{12}$$

for all $q \in V_h$.

The blood vessel Ω_v, representing the source of oxygen, is assumed to be a thin tube, with radius much smaller than the characteristic length of the three-dimensional domain. In order to avoid an excessive refinement of the mesh close to the vessel, the source term on the boundary of $\partial\Omega_v$ is treated in a multi-scale fashion, adopting the *immersed boundary* formulation proposed in [12]. In this approach, the vessel is described by a one-dimensional manifold Γ_v, representing the vessel axis (centre-line), which does not need to be fully resolved by the finite element mesh, and it is *immersed* in the three-dimensional domain, in the sense that it enters the diffusion equation (12) only as a singular flux term. In practice, the term Φ_v in equation (12) is approximated by

$$\tilde{\Phi}_v = \left(\frac{1}{J_v}(c - c_v), q\right)_{\Gamma_v} = \int_\Omega \frac{1}{J_v}(c - c_v) q\, \delta^h_{\Gamma_v}\, d\Omega. \tag{13}$$

where $\delta^h_{\Gamma_v}$ stands for a discrete approximation of the Dirac delta function of the vessel centre-line.

The main advantages of this approach is that it allows us to use a coarser spatial discretisation. In practice, the finite element mesh needs only to be refined around blood vessels, but it does not need to fully resolve the vessel geometry. Hence, the formulation can handle arbitrary vessel configurations.

3.3. Coupling with the individual-based model

3.3.1. Cell phenotype

Within the model, each cell is characterised by a particular phenotypic state, depending on the amount of oxygen available. In particular, we distinguish between *normoxic*, *hypoxic*, and *necrotic* states [see also 6, 32, 33, 36]. By default, cells are normoxic, and they remain in this state, as long as the oxygen concentration at their spatial location remains above a specified threshold (τ_{hypo}), performing aerobic metabolism. If the oxygen concentration falls below τ_{hypo}, the cell activates anaerobic metabolism (i.e., it consumes oxygen at a lower rate so that $\alpha_h < \alpha_n$), stops proliferating and acquires additional motility. The increased motility is modelled by increasing the magnitude of the random movement term, $a^r f_i(t)$, of Equation (2) by a factor v_{hypo} [see also 32]. Hypoxic cells that move into locations where oxygen levels are reverted to physoxia may revert their phenotype back to normoxic [4]; following our previous work [6], we consider that when oxygen levels rise over the hypoxia threshold (τ_{hypo}) cells

may revert to normoxic with a probability $p = 1/24$ hours. Ultimately, however, if the oxygen concentration decreases below a dramatic threshold (τ_{dead}), the cells undergo apoptosis by anoxia [32], becoming biologically inactive. These dead cells remain in the system as a part of the debris in necrotic regions and they move only as a consequence of mechanical forces.

3.4. Implementation details

The stationary equation (11) is solved numerically using a P2 finite element method implemented within the library FreeFem++ (v 3.42) [26]. In order to couple the finite element solver with the individual cell solver, the two models have to be defined on the same computational domain. However, this relies on different discretization strategies. For practical implementation, we considered a cubic domain – subdivided into smaller boxes (to simplify the search operations, see Section 2.4) – and generated a tetrahedral mesh using Gmsh (v4.4.1) [23] and TetGen (v1.5) [42].

3.4.1. Time-stepping and up-scaling of the cell distribution

As discussed in Section 3.1, the feedback of the cell model on the diffusion equation (11) is driven by the density of normoxic and hypoxic cells (as necrotic cells do not consume nutrients), which is assumed to be constant in the short time needed by the diffusion problem to reach an equilibrium.

The cell density, $\rho = \rho_n + \rho_h$, has been computed directly in the discrete finite element setting, i.e., approximating ρ as a piece-wise constant function on each mesh tetrahedra. To this end, we pre-computed a map, assigning, to each tetrahedra, the box containing its barycentre. This step allows us to efficiently evaluate the piece-wise approximation of cell density by mapping each cell from its box to a given tetrahedra, and summing up the contribution for each tetrahedra.

Another observation allows for a further gain in computational efficiency. Since the spatial configuration of the cell undergoes only limited changes between time steps, the finite element solver is not launched at each time iteration. Instead, at each time step only the up-scaled cell density (a piecewise constant function on the tetrahedral mesh) is computed and stored.

The solution to the steady diffusion equation is only updated when the relative difference (in L^2-norm) between the current density and the one used in the previous finite element iteration used is above a certain threshold. In our numerical simulations, we relaunched the finite element solver whenever the relative difference was above 5%. However, a rigorous multiscale analysis would be necessary, in order to derive an optimal scale separation strategy. This issue is subject of current investigation.

3.4.2. Individual-based treatment for vessels

Besides providing available nutrient concentration, the blood vessels are also handled within the IB model as independent geometrical entities, this is not the case in [6] and is one of the major changes to the model presented here. We

consider an adhesion-repulsion interaction model in order to model cell adhesion to vessel walls without, at least in this instance, allowing cells to penetrate the space occupied by blood vessels. From the computational point of view, vessels segments are treated as additional agents, characterised by their extrema, their orientation and their radius. Let us introduce the vectorial distance between cell and vessel surface $\mathbf{h}_{iv}$, i.e., the vector connecting the centre of cell i with vessel v, and perpendicular to the vessel axis. The cell-vessel interaction force is computed as the sum of a repulsion and an adhesive term, as:

$$\mathbf{F}_{i,v} = \left[\frac{4}{3}\hat{E}R_i^{\frac{1}{2}}\|\mathbf{h}_{iv}\|^{\frac{3}{2}} - \alpha_{\text{vessel}}S_{iv}\right]\frac{\mathbf{h}_{iv}}{\|\mathbf{h}_{iv}\|} \tag{14}$$

with $\frac{1}{\hat{E}} = \frac{1-\nu_i^2}{E_i} + \frac{1-\nu_v^2}{E_v}$ (where E_i, ν_i and E_v, ν_v denote the Young's moduli and Poisson ratios of cell i and vessel v, respectively), α_{vessel} is an adhesion coefficient and S_{iv} is the surface of cell-vessel contact, which is approximated analogously to the cell-cell adhesion surface (Equation (6)). When solving for the cell position, this contribution is added to the right-hand side of Equation (2).

3.5. Computational results

We consider a tissue sample of size $600\mu\text{m}\times400\mu\text{m}\times400\mu\text{m}$, with six vessel segments arranged as depicted in the left-hand panel of Figure 1. In the right-hand panel of Figure 1 we show the oxygen concentration without the presence of cells. The model parameters are summarised in Table 2.

Parameter	Description	Value
E_v	vessel Young's modulus	$1e{-}3\mu\text{N}/\mu\text{m}^2$
ν	vessel Poisson ratio	0.5
α_{vessel}	cell-vessel adhesion coefficient	$3.72e{-}4\mu\text{N}/\mu\text{m}^2$
$c^{(T)}$	O_2 saturation constant	2.5mmHg
α_n	normoxic consumption coefficient	0.3
α_h	hypoxic consumption coefficient	0.06
η	determines boundary condition type	0.02
J_v	coefficient for filtration term	$1e{-}3$
τ_{hypo}	hypoxia O_2 p.p. threshold	7.0mmHg
τ_{death}	necrosis O_2 p.p. threshold	0.7mmHg
v_{hypo}	hypoxic motility variance factor	10.0

Table 2: Parameter values for the vessel interactions used in simulations. The abbreviation p.p. stands for partial pressure.

In Figure 2 we give the results of a simulation of the vascularised tumour growth model after 16 000 timesteps, when the population size has reached approximately 20 000 cells. The plots show two different views of the cell population, which has been coloured according to oxygen concentration. It shows that the tumour grows between the vessel network without penetrating the vasculature and, intuitively, the cells closest to the vessel segments have higher

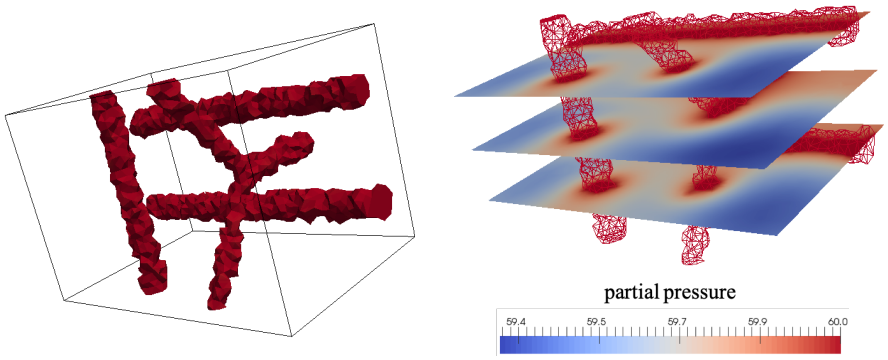

Figure 1: Left: the vessel geometry considered in the simulation. Notice that the plot shows the contour surfaces of the partial pressure equal to 60mmHg, since vessels are not explicitly resolved within the computational mesh. Right: Partial pressure field in three different cross-sections without the presence of cancer cells.

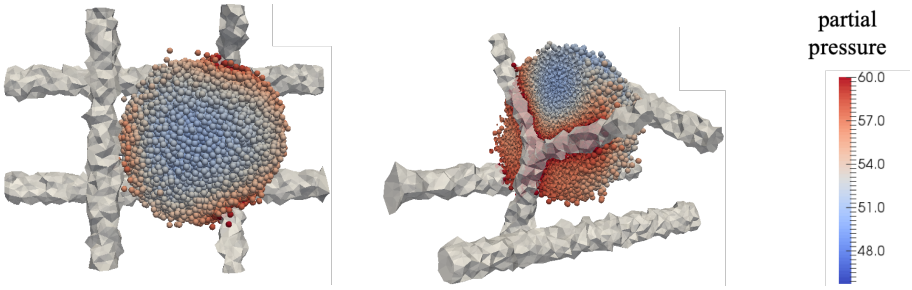

Figure 2: Cancer growth simulation after 16 000 time steps (approximately 20 000 cells). The cells are coloured according to available oxygen concentration. In the two panels we show the domain from different viewpoints.

O_2-levels. Figure 3 depicts the level curves of oxygen concentration computed with the finite element solver within the vascular tissue, showing the effect of the *sink* terms due to the cell consumption.

4. Cell-fibre interactions

While interactions with any local vasculature obviously play an important role in the growth and evolution of a solid tumour, interactions with other components of the surrounding stroma also play a key role. Fibrous connective tissue performs a wide variety of functions within the healthy body but in terms of cancer development the structure of the extra-cellular matrix (ECM) and the interaction with individual fibres of the matrix drives cell migration. Malignant cells activate the integrin migration pathway and crawl towards the protein network of the ECM. Migration through the protein network results in the

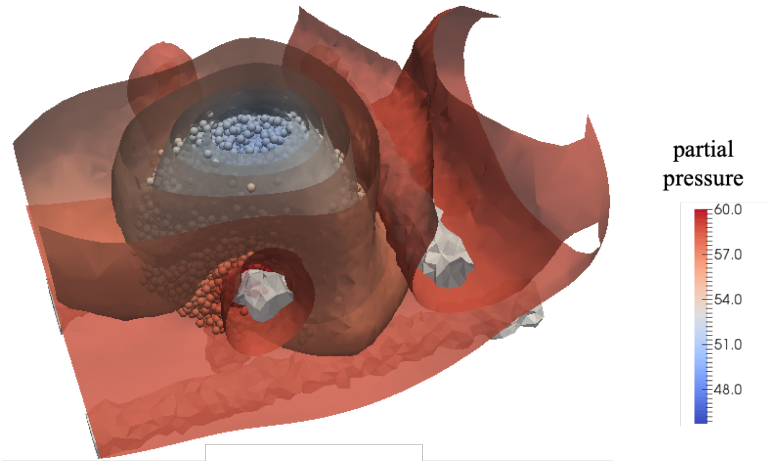

Figure 3: Cancer growth simulation after 16 000 time steps. The plot depicts the contour surfaces of the O_2 partial pressure field.

rearrangement of the ECM structure as cancer cells use the integrin pathway to cut-off the fibres and re-orient the ECM. Cell migration can happen as a collective process that presents in different ways depending on the tumour type and the nearby environment leading to different migration structures [17, 18].

In this Section, we describe an extension of the IB model presented in Section 2 that takes into account a three-dimensional fibrous ECM, where fibres of arbitrary shape and orientation interact with the individual cells.

4.1. Mathematical Model

Each individual fibre is modelled explicitly in the first instance by a thin cylinder (described by its extrema and radius), and we assume that the whole three-dimensional computational domain is filled by fibres with a given distribution of positions and orientations.

4.1.1. Forces on the cell

Let us consider a cell i in contact with a fibre f. In order to model the interaction, we assume that each cell moves in response to a fibre in two directions. In particular, a cell in contact with a fibre will feel an adhesive force, parallel to fibre orientation and a repulsive force orthogonal to the fibre (see, e.g., [11]).

The adhesive force is modelled as

$$\mathbf{F}_{\parallel} = \alpha_{\text{fibre}} \left(1 - \frac{\|\mathbf{v}_i\|}{v_{\max}}\right) \left(\frac{|\mathbf{v}_i \cdot \mathbf{l}_f|}{\|\mathbf{v}_i\|}\right)^s \mathbf{l}_f \,. \tag{15}$$

The force is directed along the normalised direction of fibre f, $\mathbf{l}_f$ (with ($\|\mathbf{l}_f\| = 1$), and depends on the normalised scalar product between $\mathbf{l}_f$ and $\mathbf{v}_i$, the velocity

of cell i. Moreover, the force depends on an adhesion coefficient, α_{fibre}, and on a threshold velocity, $v_{\max}$, which limits the pulling effect of fibres. The additional parameter $s > 0$ can be used to model additional effects which might increase ($s < 1$) or decrease ($s > 1$) the pulling effect. For the simulation showed in this work, we use $s = 1$.

Conversely, the repulsion force is modelled via an additional friction exerted by the fibre, again depending on the normalised scalar product between $\mathbf{l}_f$ and $\mathbf{v}_i$, and directed parallel to cell velocity and depending on the component of cell velocity orthogonal to the fibre:

$$\mathbf{F}_{\perp} = \beta_{\text{fibre}} \left(\frac{\|\mathbf{v}_i\|^2 - |\mathbf{v}_i \cdot \mathbf{l}_f|^2}{\|\mathbf{v}_i\|^2} \right)^r \mathbf{v}_i \,. \tag{16}$$

In (16), β_{fibre} is the friction coefficient and the exponent $r > 0$ can be used to model nonlinear effects which increase ($r < 1$) or decrease ($r > 1$) the repulsion forces. For the simulation showed in this work, we use $r = 1$. The cell-fibre interaction force is computed as the sum of the repulsion and adhesive terms, $\mathbf{F}_{i,f} = F_{\parallel} - F_{\perp}$, when solving for the cell position, this contribution is added to Equation (2).

4.1.2. Fibre degradation

A further biologically relevant aspect is the possibility that the fibres are degraded by the cells. To take this aspect into account, we include the possibility that, during the interaction between a cell and a fibre, the latter is partially or totally broken. Specifically, at present, each fibre is equipped with an additional flag variable $\delta_f \in \{0, 1\}$, equal to 1 if the fibre is degraded. For each cell in close proximity to a given fibre, f, the fibre is degraded with probability p_{contact} if the cell is moving towards the fibre and in general with probability $p_{\text{diffusion}}$. For the simulations shown in this paper very few fibres per simulation are degraded.

4.2. Implementation details

From the technical point of view, the model for the fibres is implemented within the same solver used for the cells. In particular, the `Fibre` class is a special computational agent which can interact with neighbouring `Cell` agents.

4.3. Computational results

We investigate the growth of a solid tumour as a function of fibre distribution, i.e., depending on density, orientation and interaction parameters (primarily the adhesion force). In the following simulation we consider a computational domain of size $500\mu m \times 2000\mu m \times 500\mu m$ containing 75 000 fibres. Fibre length is assumed to be normally distributed with mean 75μm and standard deviation 5μm [40], while fibre radius is set to 2μm. With these choices, we obtain a total fibre volume ratio comparable with the one used in [40]. The parameters for the fibre-cell force components are given in Table 3.

In the first simulation we show how a tumour grows oriented with fibres which are uniformly distributed aligned with the y-axis. We place a single cancer

Parameter	Description	Value
α_{fibre}	cell-fibre adhesion coefficient	$0.005 - 0.02$N
β_{fibre}	resistive coefficient orthogonal to fibre	$10^{-3}\text{Nmin}\mu\text{m}^{-1}$
$v_{\max}$	maximum fibre-induced cell velocity	$10\mu\text{mmin}^{-1}$
p_{contact}	fibre contact degradation rate (per cell)	10^{-3}min^{-1}
$p_{\text{diffusion}}$	fibre diffusion degradation rate (per cell)	10^{-6}min^{-1}

Table 3: Parameter values for the fibre-cell force components used in simulations

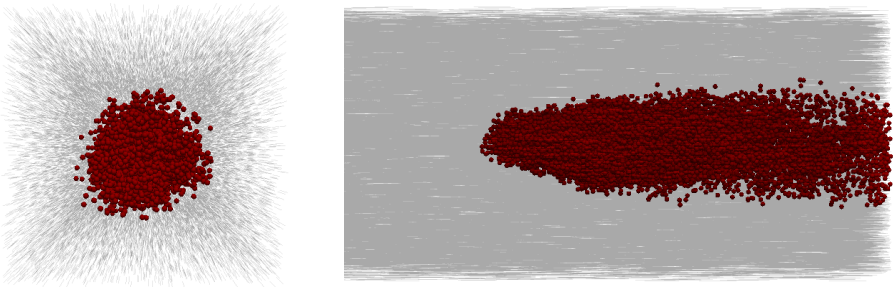

Figure 4: Example of a simulation with cell-fibre adhesion parameter set to 0.03N and using uniformly distributed fibres along the y-axis, after 9000 time steps. Cells are represented by red spheres, fibres in grey. Left: View orthogonal to the fibre orientation (xz-plane). Right: View in the yz-plane, cropped on the left side.

cell within our fibrous domain, the result after 9 000 timesteps (approximately 6 days) of a sample simulation (with a relatively high adhesion coefficient) are shown in Figure 4. Whereas in the absence of fibres we typically see a spherical tumour mass (as in Figure 2), here the growth has been stretched out along the fibrous tissue.

We investigate how the shape of the tumour changes depending on key parameters, namely, the adhesion coefficient α_{fibre}, the fibre density (number of fibres) and the variance of the fibre orientation distribution. For different simulation settings, we run 200 simulations in each case, computing the final shape of the tumour with the quantity

$$\delta = \frac{\sqrt{3}a_y}{\sqrt{a_x^2 + a_y^2 + a_z^2}} \tag{17}$$

where a_y is the length of the tumour mass in the y direction etc. As such δ measures the anisotropy along the y-axis, which is the main axis of orientation of fibres. The results are shown in Figure 5. We show that if we increase either the cell-fibre adhesion coefficient or the number of fibres the tumour grows preferentially in the y-direction. Conversely as we increase the variance of the fibre orientation the tumour grows more isotropically.

IIn the next numerical test we investigate the motion of a single cell (non-proliferating) within a given anisotropic fibre distribution. The cell is placed

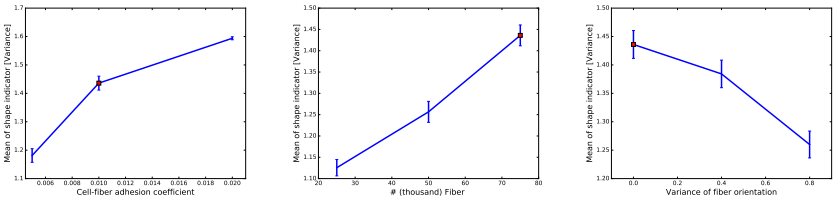

Figure 5: The shape of the distribution of cells within the domain, given by Equation (17). We vary the fibre adhesion coefficient, number of fibres and variance of fibre orientation in the left, middle and right plots, respectively. In each plot, the red square indicates the baseline simulation ($\alpha_{\text{fibre}} = 0.01$N). The y-axis represents the mean value of the indicator, δ, for the set of simulations, while the vertical error bar corresponds to the variance.

at (250,50,250), while fibres are generated with a fibre volume ratio as above (i.e. 75 000 fibres over a domain $500\mu m \times 2000\mu m \times 500\mu m$), and oriented along the y-axis. We run 100 simulations for 10 000 timesteps, monitoring the path of the cell within the fibrous domain. The results are shown in Figure 6. We observe that the y-orientated fibrous distribution induces the cell to move along the y-axis parallel to the direction of the fibres (Figure 6 , top left), with a smaller diffusive effect along the x and z axes (Figure 6, top right). The bottom panel of 6 compares the mean and variance of the displacement along each axial direction, showing greater movement along y.

In the final numerical test, we investigate how the statistics of the motion of a single cell (non proliferating and placed at (250,50,250)) changes as we vary parameters affecting the interaction between the cell and the fibrous tissue. In particular, we monitor the dispersive behavior of the motion, i.e., the difference between the movement along the y-axis (which is the preferential orientation of the fibres) and in its orthogonal plane. We run 100 simulations for 10 000 timesteps, monitoring the path of the cell within the fibrous domain.

The results (showing the path of the cell for a single run of the simulation and the general dispersion behaviour for all 100 runs) are shown in Figure 7. The top figures show the results if we reduce the cell-fibre adhesion from 0.03N to 0.01N, hence decreasing the "pulling" effect in the direction of the fibres. We observe that the cells still predominantly move in the y-direction (with a smaller diffusive effect in the x- and z-directions) but do not move as far into the domain as observed in Figure 6. The small diffusive effect in the x- and z-directions remains as in Figure 6. The middle figures in Figure 7 show the effect of reducing fibre density (decreasing the number of fibres from 75 000 to 25 000). In this case cells come into contact with fewer fibres and as such the "pull" the cell feels in the direction of the fibres is again reduced, yielding similar results as the ones shown in the top panel of 7. Finally, the bottom figures in Figure 7 show the effect of increasing the variance of fibre orientation distribution. Specifically, instead of a uniformly oriented fibre distribution (along the y-direction), we sample fibre orientation from a normal distribution with mean $(0, 1, 0)$ (along y-direction) and variance of elevation and azimuthal angles equal to 0.8. Hence, fibres are

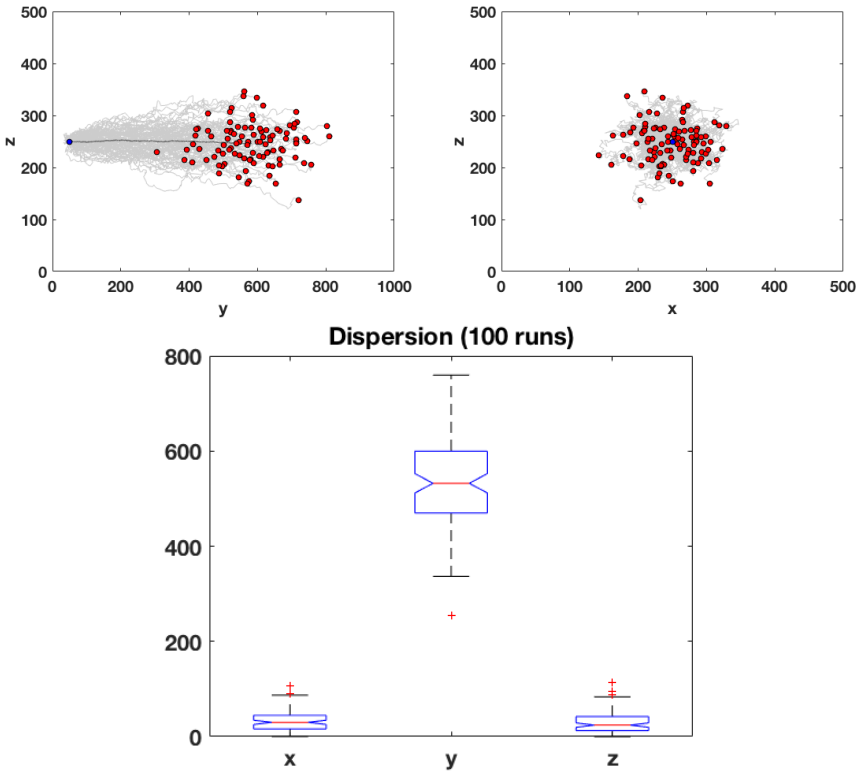

Figure 6: Results of 100 simulations of a single cell (initial position at (250,50,250)) moving within a fibrous domain. Top Panel: the initial position is indicated by a blue circle, while final positions (for each simulation) are marked in red. The trajectories are indicated by the light grey lines. Left: y-z plane. Right: x-z plane. In the left hand plot we indicate the mean path with the dark grey line. Bottom Panel: The dispersion in each of the axial directions for the 100 simulations.

now oriented in different directions, although there remains a preference for fibres oriented in the y-direction. In this case the cells continue to feel a strong "pull" predominantly along the y-axis although slightly less so than in Figure 6, and the variance of the motion along the x and z-axes directions also increases.

5. Discussion and Conclusions

The evolution from the first mathematical models of biological systems to the present computational approaches indicates both the difficulties that science has faced in this field but also the great advances that have been made. As experimentalists come to a deeper understanding of cellular behaviour as multiscale complex systems of interactions, the modelling community is endeavouring to reconstruct the biology ever more faithfully. In the last few decades particularly, a range of powerful computational exploratory tools has been created.

In this "proof of concept" paper we have detailed our *in silico* IB model of solid tumour growth within the tumour microenvironment in which cancer cells interact not only with each other but also with the local vasculature and fibrous tissue. The code has been developed from that in [6] to include these vessel/fibre interactions. We have shown that the basic model can reproduce important key biological aspects. Tumour shape, for example, is driven both by fibre orientation in the domain as seen in Section 4 and local vascular structure as seen in Section 3. Cell migration is also led by interactions with the environment as cells move preferentially along fibres (Section 4) or in search of sources of nutrient (namely oxygen) due to oxygen phenotypic profiles which is dealt with extensively in [6].

The model as it stands presents many significant avenues for further development, and we detail a selection of these here. With regards to our remark in Section 2.3 there are additional modifications we could make to tweak our model to investigate other relevant biological factors, such as changing the growth rate of cells to be dependent on nutrient availability. With regards to cell-vessel interaction we seek to couple the model with the angiogenesis model of [5], in such a way that not only can we model the interactions between cells and existing vasculature but also that we can investigate solid tumour dynamics under vascularisation. This would involve modelling the diffusion of, for example, vascular endothelial growth factor (VEGF) from hypoxic cancer cells into the surrounding tissue. VEGF is a protein produced by cancer cells that provide the initial signals for endothelial cells to form new blood vessels. We intend to model the production and diffusion of VEGF in an analogous way to the modelling of oxygen diffusion in Section 3.

Since blood vessels are now physically represented in the IB model this would permit us to couple the cell model with a flow model, taking into account the pressure of the cells on the vessel boundary to model, for example, vessel collapse. Equally, we could develop the physical interactions between cells and vessels to incorporate the possibility of intra- and extra-vasation of cells into and out of blood vessels. This would be a first major stepping stone in piecing

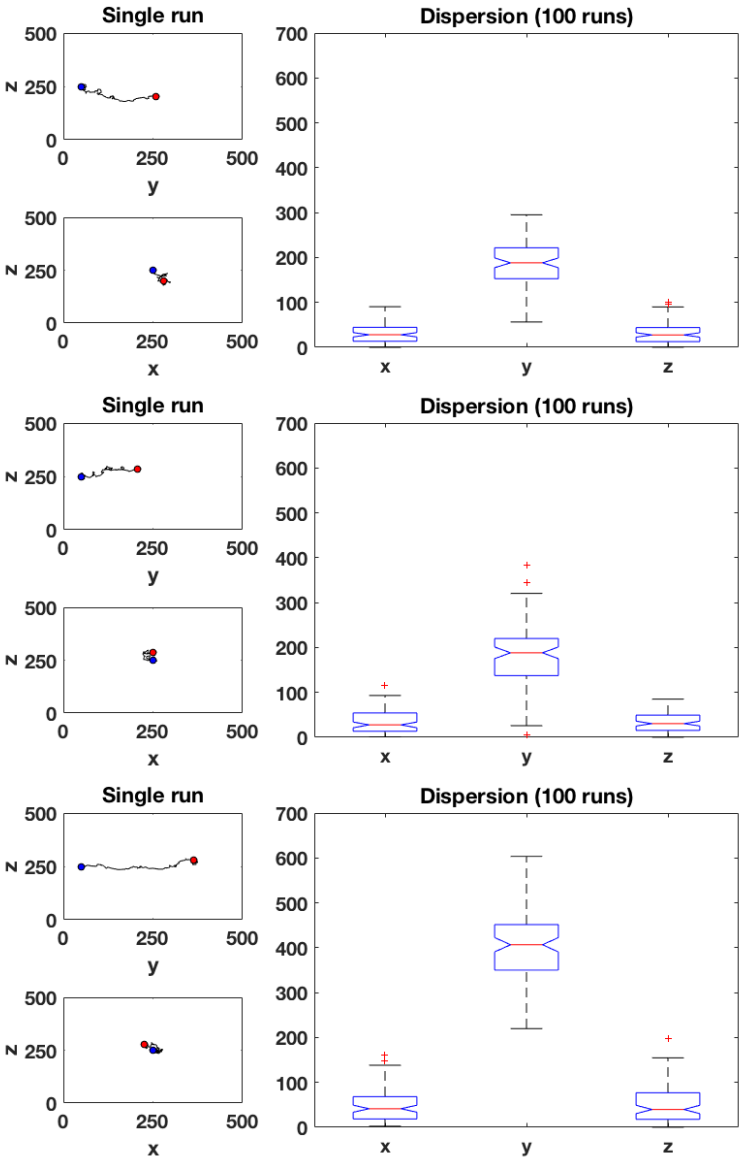

Figure 7: Results of 100 simulations of a single cell (initial position at $(250, 50, 250)$) moving within a fibrous domain under changes to parameters. Left Panels: a single cell path shown in the y-z and x-z planes; the initial position is indicated by a blue circle, and the final position is marked by a red circle. Right Panel: The dispersion in each of the axial directions for the 100 simulations. Top Panel: reduction of the fibre adhesion parameter α_{fibre}. Middle Panel: reduction in the number of fibres. Bottom Panel: increase in the fibre orientation variance.

together an individual-based force-based model of metastatic spread. With the ability to model both local invasion and metastasis we will have a better understanding of one of cancer's most deadly *Hallmarks* [24, 25] and a platform from which to investigate ways of stopping the spread of the disease.

The numerical tests related to cell-fibre interaction presented in this paper are limited to a single migrating cell. Besides serving as a preliminary validation, the interest of studying a single cell migration can be found in the experimental literature. For example, Friedl and co-workers have carried out in vivo experiments looking at single cells migrating through collagen fibres both in normal and cancerous tissue [20, 17, 45, 18]. Additionally there is the possibility of comparing the simulations with in vitro experiments using digital holographic imaging which tracks the movement of independent cells (see, e.g., [7, 15]). Ongoing development concerns the incorporation of more detailed aspects of ECM re-modelling by cancer cells. As much as cells are driven along fibres, fibres can also be pushed and re-oriented by contact with cells. We have already included a first-step model of fibre degradation whereby fibres that are in contact with cells are subject to a rate of degradation. In order to make this aspect more biologically relevant we could instead couple it to a reaction-diffusion equation for matrix metalloproteinases (MMPs) and other matrix degrading enzymes - in a similar way to the modelling of oxygen shown in Section 3. MMPs are enzymes released by cancer cells which are capable of degrading key components of the ECM such as collagen fibres.

Nonetheless, we currently have a novel individual-based model of solid tumour growth which can replicate key aspects of growth and development and which forms a foundation to build upon. What is important now is to take our current model from an exploratory tool to a quantitative, predictive one.

Acknowledgements

MAJC and CKM gratefully acknowledge the support of EPSRC Grant No. EP/N014642/1 (EPSRC Centre for Multiscale Soft Tissue Mechanics - With Application to Heart & Cancer).

[1] A. R. A. Anderson, K. A. Rejniak, P. Gerlee, and V. Quaranta. Modelling of cancer growth, evolution and invasion: Bridging scales and models. *Math Model Nat Phenom*, 2(3):1–29, 2007.

[2] A. Araujo, L. M. Cook, C. C. Lynch, and D. Basanta. An integrated computational model of the bone microenvironment in bone-metastatic prostate cancer. *Cancer Res*, 74(9):2391–2401, 2014.

[3] Ahmad A.S., N. Ormiston-Smith, and P.D. Sasieni. Trends in the lifetime risk of developing cancer in great britain: Comparison of risk for those born in 1930 to 1960. *Br J Cancer*, 112(5):943–947, 2015.

[4] Pushpak N. Bhandari, Yi Cui, Bennett D. Elzey, Craig J. Goergen, Christopher M. Long, and Joseph Irudayaraj. Oxygen nanobubbles revert hypoxia by methylation programming. *Scientific Reports*, 7(1):9268, 2017.

[5] A. Boujelben, M. Watson, S.R. McDougall, Y-F Yen, E.R. Gerstner, C. Catana, T. Deisboeck, T.T. Batchelor, D. Boas, B. Rosen, J. Kalpathy-Cramer, and M.A.J. Chaplain. Multimodality imaging and mathematical modelling of drug delivery to glioblastomas. *Interface Focus*, 6:20160039, 2016.

[6] A. Caiazzo and I. Ramis-Conde. Multiscale modelling of palisade formation in gliobastoma multiforme. *J Theor Biol*, 383:145–156, 2015.

[7] L.V. Croft, J.A. Mulders, D.J. Richard, and K. OBÌyrne. Digital Holographic Imaging as a Method for Quantitative, Live Cell Imaging of Drug Response to Novel Targeted Cancer Therapies. In *Batra J., Srinivasan S. (eds) Theranostics. Methods in Molecular Biology, Humana, New York, NY*, volume 2054, pages 171–183, 2019.

[8] M. Cytowski and Z. Szymańska. Large scale parallel simulations of 3-d cell colony dynamics. *IEEE Comput Sci Eng*, 16(5), 2014.

[9] M. Cytowski and Z. Szymańska. Enabling large scale individual-based modelling through high performance computing. In *ITM Web of Conferences*, volume 5, page 00014, 2015.

[10] M. Cytowski and Z. Szymańska. Large scale parallel simulations of 3-d cell colony dynamics. ii. coupling with continuous description of cellular environment. *Comput Sci Eng*, 17:44–48, 2015.

[11] J. C. Dallon, J. A. Sherratt, and P. K. Maini. Mathematical modelling of extracellular matrix dynamics using discrete cells: fiber orientation and tissue regeneration. *J Theor Biol*, 199:449–471, 1999.

[12] C. D'Angelo and A. Quarteroni. On the coupling of 1d and 3d diffusion-reaction equations: application to tissue perfusion problems. *Math Models Methods Appl Sci*, 18(08):1481–1504, 2008.

[13] D. Drasdo and S. Hoehme. A single-cell-based model of tumor growth in vitro: monolayers and spheroids. *Phys biol*, 2:133–47, 2005.

[14] D. Drasdo, S. Hoehme, and M. Block. On the role of physics in the growth and pattern formation of multicellular systems: What can we learn from individual-cell based models? *J Statist Phys*, 128:287–345, 2007.

[15] F. Dubois, C. Yourassowsky, O. Monnom, J. Legros, O. Debeir, P. Ham, R. Kiss, and C. Decaestecker. Digital holographic microscopy for the three-dimensional dynamic analysis of in vitro cancer cell migration. *J Biomed Optics*, 11:054032, 2006.

[16] J. Ferlay, I. Soerjomataram, R. Dikshit, S. Eser, C. Mathers, M. Rebelo, D.M. Parkin, and Forman D. Bray F. Cancer incidence and mortality worldwide: sources, methods and major patterns in globocan 2012. *Int J Cancer*, 136(5):E359–E386, 2015.

[17] P. Fiedl and K. Wolf. Tumour-cell invasion and migration: diversity and escape mechanisms. *Nat Rev Cancer*, 3(5):362–374, 2003.

[18] P. Fiedl and K. Wolf. Proteolytic interstitial cell migration: a five-step process. *Cancer Metastasis Rev*, 28(1-2):129–135, 2009.

[19] L. C. Franssen, T. Lorenzi, A. F. Burgess, and M. A. J. Chaplain. A mathematical framework for modelling the metastatic spread of cancer. *Bull Math Biol*, 81(6):1965–2010, 2019.

[20] P. Friedl, K. S. Zänker, and E-B. Bröcker. Cell migration strategies in 3-d extracellular matrix: Differences in morphology, cell matrix interactions, and integrin function. *Microscopy Research and Technique*, 43:369–378, 1998.

[21] J. Galle, G. Aust, G. Schaller, T. Beyer, and D. Drasdo. Individual cell-based models of the spatial-temporal organization of multicellular systems—achievements and limitations. *Cytom Part A*, 69:704–10, 2006.

[22] J. Galle, M. Loeffler, and D. Drasdo. Modeling the effect of deregulated proliferation and apoptosis on the growth dynamics of epithelial cell populations in vitro. *Biophys J*, 88(1):62–75, 2005.

[23] C. Geuzaine and J.-F. Remacle. Gmsh: a three-dimensional finite element mesh generator with built-in pre- and post-processing facilities. *Int J Num Methods Engrn*, 79(11):1309–1331, 2009.

[24] D. Hanahan and R. A Weinberg. Hallmarks of cancer. *Cell*, 100:57–70, 2000.

[25] D. Hanahan and R. A Weinberg. Hallmarks of cancer: the next generation. *Cell*, 144:646–674, 2011.

[26] F. Hecht. New development in freefem++. *J Numer Math*, 20(3-4):251–265, 2012.

[27] H. Hertz. Ueber die berührung fester elastischer körper (on the contact of elastic solids). *J Reine Angew Mat*, 92:156–171, 1882.

[28] W.-Y. Hu, W.-R. Zhong, L. Wang, F.-H.and Li, and Y.-Z. Shao. In silico synergism and antagonism of an anti-tumour system intervened by coupling immunotherapy and chemotherapy: a mathematical modelling approach. *Bull Math Biol*, 74(2):434–452, 2012.

[29] J. N. Kather, J. Poleszczuk, M. Suarez-Carmona, J. Krisam, P. Charoentong, N. A. Valous, C. A. Weis, L. Tavernar, F. Leiss, E. Herpel, F. Klupp, A. Ulrich, M. Schneider, A. Marx, D. J´ager, and N. Halama. In silico modeling of immunotherapy and stroma-targeting therapies in human colorectal cancer. *Cancer Res*, 77(22):6442–6452, 2017.

[30] F. R. Macfarlane, T. Lorenzi, and M. A. J. Chaplain. Modelling the immune response to cancer: an individual-based approach accounting for the difference in movement between inactive and activated t cells. *Bull Math Biol*, 80:1539–1562, 2018.

[31] P. Macklin, M. Edgerton, A. Thompson, and V. Cristini. Patient-calibrated agent-based modelling of ductal carcinoma in situ (dcis): from microscopic measurements to macroscopic predictions of clinical progression. *J Theor Biol*, 301:122–170, 2012.

[32] A. Martínez-González, G. F. Calvo, L. A. Pérez-Romasanta, and V. M. Pérez-García. Hypoxic cell waves around necrotic cores in glioblastoma: a biomathematical model and its therapeutic implications. *Bull Math Biol*, 74(12):2875–96, 2012.

[33] A. Martínez-González, M. Durán-Prado, G. F. Calvo, F. J. Alcaín, L. A. Pérez-Romasanta, and V. M. Pérez-García. Combined therapies of antithrombotics and antioxidants delay in silico brain tumor progression. *Math Med & Biol*, 32(239-262), 2015.

[34] J. Metzcar, Y. Wang, R. Heiland, and P. Macklin. A review of cell-based computational modeling in cancer biology. *JCO Clinical Cancer Informatics*, 3:1–13, 2019.

[35] F. Pappalardo, S. Musumeci, and S. Motta. Modeling immune system control of atherogenesis. *Bioinformatics*, 24:1715–1721, 2008.

[36] R. Pardo, A. Martínez-González, and V. M. Pérez-García. Nonlinear ghost waves accelerate the progression of high-grade brain tumors. *Commun Nonlinear Sci Numer Simulat*, 39:360–380, 2016.

[37] I. Ramis-Conde, M. A. J. Chaplain, A. R. A. Anderson, and D. Drasdo. Multi-scale modelling of cancer cell intravasation: the role of cadherins in metastasis. *Phys Biol*, 6(1):016008, 2009.

[38] I. Ramis-Conde, D. Drasdo, A. R. A. Anderson, and M. A. J. Chaplain. Modeling the influence of the e-cadherin-beta-catenin pathway in cancer cell invasion: a multiscale approach. *Biophys J*, 95(1):155–65, 2008.

[39] K. A. Rejniak, S. E. Wang, N. S. Bryce, H. Chang, B. Parvin, J. Jourquin, L. Estrada, J. W. Gray, C. L. Arteaga, A. M. Weaver, V. Quaranta, and A. R. A. Anderson. Linking changes in epithelial morphogenesis to cancer mutations using computational modeling. *PLoS Comput Biol*, 6(8):e1000900, 2010.

[40] D. K. Schlüter, I. Ramis-Conde, and M. A. J. Chaplain. Computational modeling of single-cell migration: the leading role of extracellular matrix fibers. *Biophys J*, 103:1141–1151, 2012.

[41] D. K. Schlüter, I. Ramis-Conde, and M. A. J. Chaplain. Multi-scale modelling of the dynamics of cell colonies: insights into cell-adhesion forces and cancer invasion from in silico simulations. *J R Soc Interface*, 12:20141080, 2015.

[42] H. Si. Tetgen, a delaunay-based quality tetrahedral mesh generator. *ACM Trans Math Softw*, 41(2):11:1–11:36, February 2015.

[43] D. W. Thompson. *On Growth and Form.* Cambridge University Press, 1917.

[44] P. Van Liedekerke, A. Buttenschön, and D. Drasdo. Off-lattice agent-based models for cell and tumor growth: numerical methods, implementation, and applications. In *Numerical methods and advanced simulation in biomechanics and biological processes*, pages 245–267. London, UK; San Diego, CA; Cambridge, MA; Oxford, UK: Elsevier Academic Press, 2018.

[45] K. Wolf, Y. I. Wu, Y. Liu, J. Geiger, E. Tam, C. Overall, M. S. Stack, and P. Friedl. Multi-step pericellular proteolysis controls the transition from individual to collective cancer cell invasion. *Nat Cell Biol*, 9(8):893–904, 2007.

[46] L. Zhang, C. G. Strouthos, Z. Wang, and T. S. Deisboeck. Simulating brain tumor heterogeneity with a multiscale agent-based model: Linking molecular signatures, phenotypes and expansion rate. *Math Comput Model*, 49(1-2):307–319, 2009.